

High Probability of Detecting Lensed Supermassive Black Hole Binaries by LISA

ZUCHENG GAO,¹ XIAN CHEN,^{1,2} YI-MING HU,³ JIAN-DONG ZHANG,³ AND SHUNJIA HUANG³

¹*Astronomy Department, School of Physics, Peking University, Beijing 100871, P. R. China*

²*Kavli Institute for Astronomy and Astrophysics at Peking University, Beijing 100871, P. R. China*

³*TianQin Research Center for Gravitational Physics and School of Physics and Astronomy, Sun Yat-sen University (Zhuhai Campus), Zhuhai 519082, P. R. China*

ABSTRACT

Gravitational lensing of gravitational waves (GWs) is a powerful probe of the matter distribution in the universe. Here we study the lensing effect induced by dark matter (DM) halos on the GW signals from merging massive black holes, and we revisit the possibility of detection using the Laser Interferometer Space Antenna (LISA). In particular, we include the halos in the low-mass range of $10^5 - 10^9 M_\odot$ since they are the most numerous according to the cold DM model. In addition, we employ the matched-filtering technique to search for weak diffraction signatures when the MBHBs have large impact parameters ($y \sim 10^2$). We find that about (20 – 40)% of the MBHB in the mass range of $10^5 - 10^6 M_\odot$ and the redshift range of 4 – 10 should show detectable wave-optics effects. The uncertainty comes mainly from the mass function of DM halos. Not detecting any signal during the LISA mission would imply that DM halos are significantly more massive than $10^8 M_\odot$.

Keywords: gravitational waves — gravitational lensing: strong — dark matter

1. INTRODUCTION

Gravitational lensing events are unique probes of the distribution of matter in the universe (Schneider et al. 1992). Like light, gravitational waves (GWs) could also be lensed by intervening matter (Lawrence 1971; Cyrancki 1974; Sonnabend 1979; Marković 1993). The prospect of detecting the lensing of GWs is promising given the increasing number of GW events discovered in the recent years by the Laser Interferometer Gravitational-wave Observatory (LIGO) and the Virgo detectors (Abbott et al. 2016, 2019; Abbott et al. 2020).

One major difference between GW and light is that the former usually has a much longer wavelength. For example, LIGO/Virgo are sensitive to the GWs with a wavelength of $\mathcal{O}(10^4)$ km. It is comparable to or longer than the characteristic sizes of many astrophysical objects, such as stars or intermediate-massive black holes (IMBHs). If lensed by these objects, the GWs in the LIGO/Virgo band would behave like light in the wave-optics limit (Ohanian 1974; Bontz & Haugan 1981;

Nakamura 1998; Nakamura & Deguchi 1999). In this case, wave diffraction would modify the amplitude and phase of the GWs, producing a characteristic “beating pattern” in the frequency domain of the waveform (Takahashi & Nakamura 2003). In addition, the wave-optics effect could also smear the plane of GW polarization (Cusin & Lagos 2020) and produce beat patterns in the time-domain waveform (Yamamoto 2005; Hou et al. 2020). These effects, in principle, could allow LIGO/Virgo to detect massive stars, IMBHs, and the dense cores of globular clusters and dark-matter (DM) halos (Moylan et al. 2008; Cao et al. 2014; Takahashi 2017; Christian et al. 2018; Dai et al. 2018; Diego et al. 2019; Jung & Shin 2019; Liao et al. 2019; Meena & Bagla 2020; Oguri & Takahashi 2020). However, so far no strong evidence of lensing effects has been officially reported by LIGO/Virgo (Hannuksela et al. 2019), suggesting that the lensing probability is relatively low.

The Laser Interferometer Space Antenna (LISA) is a future space-based mission aiming at detecting the GWs in the milli-Hertz (mHz) band (Amaro-Seoane et al. 2017). One of its major targets is the merger of two massive black holes (MBHs), preferentially in the mass range of $10^4 \sim 10^7 M_\odot$. Because of the superb sensitivity, LISA could detect MBH mergers up to a redshift of

phy15gzc@pku.edu.cn

xian.chen@pku.edu.cn

20 with a signal-to-noise ratio (SNR) as high as $10^2 - 10^3$ (Amaro-Seoane et al. 2017). Such a high redshift suggests that gravitational lensing by the large-scale structure is no longer negligible for LISA (Takahashi 2006; Yoo et al. 2007). The long wavelength and high SNR also indicate that the diffraction effects in the wave-optics limit, which is relatively weak for LIGO/Virgo sources, may become significant for LISA.

For LISA, the lenses which produce the diffraction effects are mainly low-mass dark-matter (DM) halos, as well as the subhalos in massive main halos (Takahashi & Nakamura 2003; Takahashi 2004). Takahashi & Nakamura (2003) considered the DM halos in the mass range of $10^9 \sim 10^{12} M_\odot$ and estimated that the lensing probability for each MBH merger in the LISA band is about $10^{-4} \sim 10^{-3}$. However, the cold DM (CDM) model predicts that the most abundant halos are those in the mass range of $10^6 \sim 10^9 M_\odot$ (e.g. Cooray & Sheth 2002; Han et al. 2016). These small halos are not included in the calculation of Takahashi & Nakamura (2003). Moreover, Takahashi & Nakamura (2003) imposed a maximum impact parameter $y = 3$ for the sources, to ensure a strong, detectable diffraction effect. This criterion, however, may be too strict. The high SNR of LISA sources would enable us to detect weak lensing signals even when the impact parameter is larger. For this reason, the lensing probability could have been significantly underestimated in the past.

Motivated by the importance of the wave-optics effects for LISA sources, we revisit the calculation of the lensing probability for the MBH binaries in the LISA band. In particular, we improve the lens model by including the halos and subhalos at the lower mass end and we also adopt the matched-filtering technique to search for weak lensing signals. We remark that although the calculation is based on LISA, the conclusion also applies to space-borne GW missions with slightly different frequency coverage, such as TianQin (Mei et al. 2020). The paper is organized as follows. In Section 2, we describe our method, including the calculation of the lensing signal in the wave-optics limit, the mass function of halos and subhalos, the probability of lensing, as well as the matched-filtering technique. Then in Section 3 we quantify the difference between the lensed and unlensed signals and derive a criterion for detecting the diffraction effect. Using this criterion, we estimate the lensing probability for the MBH mergers in the LISA band in Section 4. We discuss the importance of DM models in Section 5 and conclude in Section 6. Throughout the paper, we assume a flat Λ CDM cosmology with the parameters $\Omega_m = 0.27$, $\Omega_\Lambda = 0.73$,

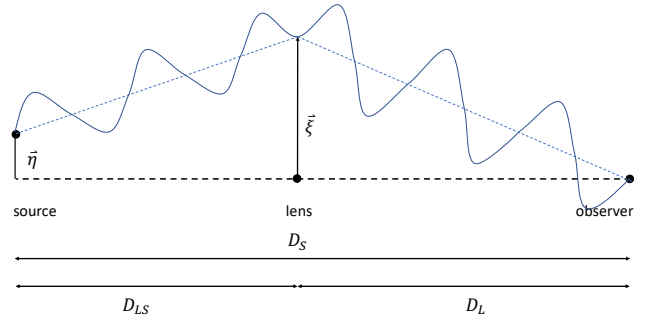


Figure 1. Physical picture of GW lensing. The vectors $\boldsymbol{\eta}$ and $\boldsymbol{\xi}$ denote the two positions on the source plane and on the lens plane. For illustrative purposes the two vectors are aligned but in principle they are not. The angular diameter distances D_L , D_S , and D_{LS} are measured in the rest frame of the observer.

$H_0 = 72 \text{ km s}^{-1} \text{ Mpc}^{-1}$, $\sigma_8 = 0.9$. Therefore, in our work $h := H_0 / (100 \text{ km s}^{-1} \text{ Mpc}^{-1}) = 0.72$.

2. METHOD

2.1. Lensing Model

For simplicity, we assume a singular isothermal sphere (SIS) profile for our DM halos and subhalos. In this case, we can follow Takahashi & Nakamura (2003) to model the diffraction of GWs. Using a more realistic Navarro-Frenk-White (NFW) profile usually leads to a slightly smaller magnification factor (Takahashi & Nakamura 2003).

The basic picture of lensing of GWs is illustrated in Figure 1, where D_L , D_S , and D_{LS} denote the angular diameter distances to the lens, to the source, and their difference. All these quantities are measured in the frame of the observer. Using these distances, the Einstein radius ξ_0 on the lens plane can be expressed with $\xi_0 = 4\pi\sigma_v^2 D_L D_{LS} / c^2 D_S$, where σ_v is the velocity dispersion of the lens.

The magnification factor is defined as

$$F(\omega, \boldsymbol{\eta}) := \frac{\tilde{\phi}_{obs}^L(\omega, \boldsymbol{\eta})}{\tilde{\phi}_{obs}(\omega, \boldsymbol{\eta})}, \quad (1)$$

where $\tilde{\phi}_{obs}^L(\omega, \boldsymbol{\eta})$ and $\tilde{\phi}_{obs}(\omega, \boldsymbol{\eta})$ are the lensed and unlensed gravitational wave amplitudes in the Fourier space, ω is the observed angular frequency of the GW, and $\boldsymbol{\eta}$ is the position vector on the source plane (“impact parameter” hereafter). Taking the cosmological redshift into account, the magnification factor can be calculated with

$$F(\omega, \boldsymbol{\eta}) = \frac{\omega(1+z_L)D_S}{2\pi i D_L D_{LS}} \int d^2\xi \exp[i\omega(1+z_L)t_d(\boldsymbol{\xi}, \boldsymbol{\eta})], \quad (2)$$

where z_L is the redshift of the lens and t_d is the time delay caused by lensing. The time delay can be computed with

$$t_d(\boldsymbol{\xi}, \boldsymbol{\eta}) = \frac{D_L D_S}{2D_{LS}} \left| \frac{\boldsymbol{\xi}}{D_L} - \frac{\boldsymbol{\eta}}{D_S} \right|^2 - \hat{\psi}(\boldsymbol{\xi}) + \hat{\phi}_m(\boldsymbol{\eta}), \quad (3)$$

where $\hat{\phi}_m(\boldsymbol{\eta})$ denotes the arrival time of the unlensed GW, which is approximately $D_S[1 + |\boldsymbol{\eta}/D_S|^2/2]/c$, and $\hat{\psi}$ is the deflection potential which solves the equation

$$\nabla_{\boldsymbol{\xi}}^2 \hat{\psi}(\boldsymbol{\xi}) = 8\pi \Sigma(\boldsymbol{\xi}), \quad (4)$$

with $\nabla_{\boldsymbol{\xi}}^2$ the two-dimensional Laplacian and $\Sigma(\boldsymbol{\xi})$ the mass surface density of the lens.

For the purpose of numerical calculation, we define the dimensionless positions as

$$\mathbf{x} = \frac{\boldsymbol{\xi}}{\xi_0}; \quad \mathbf{y} = \frac{D_L}{\xi_0 D_S} \boldsymbol{\eta}. \quad (5)$$

The corresponding dimensionless frequency is

$$w = 4GM_L(1 + z_L)\omega/c^3, \quad (6)$$

where M_L is the so-called ‘‘lens mass’’, which is defined as the mass enclosed by a circle of the Einstein radius in the lens plane. In the SIS model, we have $M_L = 4\pi^2 \sigma_v^4 D_L D_{LS} / (GD_S c^2)$ (Appendix A). Using the above nondimensional quantities, the time delay can be rewritten as

$$\begin{aligned} T(\mathbf{x}, \mathbf{y}) &= \frac{D_L D_{LS}}{D_S} \xi_0^{-2} t_d(\boldsymbol{\xi}, \boldsymbol{\eta}) \\ &= \frac{1}{2} |\mathbf{x} - \mathbf{y}|^2 - \frac{D_L D_{LS}}{D_S} \xi_0^{-2} \hat{\psi}(\boldsymbol{\xi}) + \frac{D_L D_{LS}}{D_S} \xi_0^{-2} \hat{\phi}_m(\boldsymbol{\eta}). \end{aligned} \quad (7)$$

It follows that the nondimensional amplification factor is

$$F(w, \mathbf{y}) = \frac{w}{2\pi i} \int d^2x \exp[iwT(\mathbf{x}, \mathbf{y})]. \quad (8)$$

In the SIS model the last equation can be calculated with

$$\begin{aligned} F(w, \mathbf{y}) &= -iw e^{iwy^2/2} \int_0^\infty dx x J_0(wxy) \times \\ &\quad \exp[iw(\frac{1}{2}x^2 - x + \phi_m(y))], \end{aligned} \quad (9)$$

where $\phi_m(y) = y + 1/2$ and J_0 is the zeroth-order Bessel function. The corresponding amplification factor $|F|$ and phase-change factor θ_F are

$$|F| = \sqrt{FF^*}, \quad \theta_F = -i \ln[F/F^*], \quad (10)$$

where F^* is the complex conjugate of F .

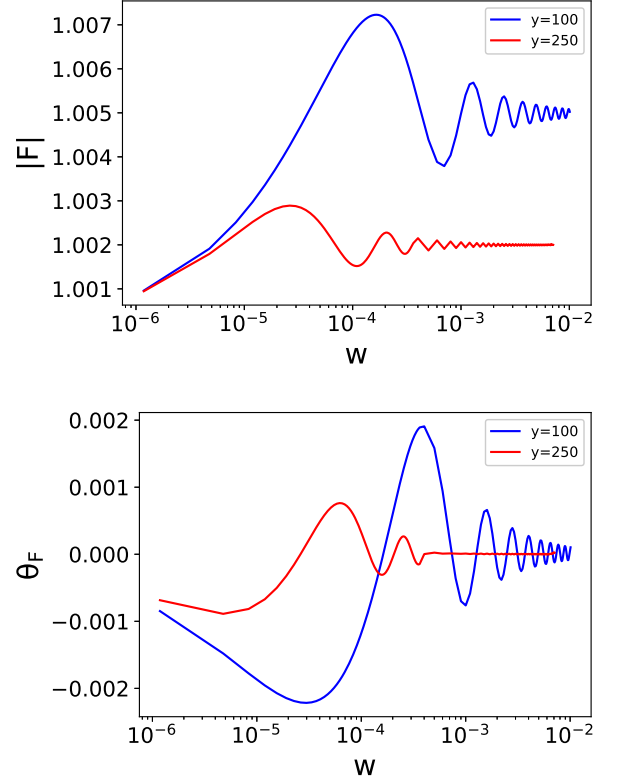


Figure 2. The amplification factor (upper panel) and the phase-change factor (lower panel) as a function of the dimensionless frequency according to the SIS model. Different lines correspond to different impact parameters (y).

Figure 2 shows the dependence of $|F|$ and θ_F on the dimensionless frequency w and impact factor y . We notice three results which are important for the later estimation of the lensing probability.

First, the amplification factor $|F|$ in general decreases with increasing impact parameter y . However, even when y is relatively large, e.g., $y = 250$, the amplification factor converges to the value in the geometric limit and is not 1, and the phase-change factor does not vanish. The implication is that even though the wave-optics effect is weak, it may still be detectable if the SNR of the event is sufficiently large. We will study the criterion for detecting such a weak signal in the later sections. The previous works, however, normally adopt an upper limit between $y = 1$ and 10 to estimate the lensing probability (e.g., Takahashi & Nakamura 2003). Such a small value could cause an underestimation of the number of lensing events.

Second, when y is fixed, both $|F|$ and θ_F could vary significantly due to the change of w . In particular, the critical value of y , above which the diffraction effect becomes undetectable, depends on w , which, according to

Equation (6), depends on the lens mass, lens redshift, and the GW frequency. We will take such a dependence into account in the following sections. These results indicate that it is oversimplified to use an single value of y to estimate the lensing probability in the diffraction limit, as is often the case in the previous works.

Third, the peaks of the amplification factor and the phase-change angles shift to smaller w as y increases. As a result, for large impact parameters, i.e., $y = 100 - 250$, the wave-optics effect appears the most significant at a small value of frequency, e.g., $w \sim (10^{-5} - 10^{-3})$. Such a small dimensionless frequency corresponds to a low-mass lens according to Equation (6), which is about

$$M_L(1 + z_L) \simeq 800 M_\odot \left(\frac{w}{10^{-4}} \right) \left(\frac{f}{10^{-3} \text{Hz}} \right)^{-1}. \quad (11)$$

The corresponding halo mass is also small, about $10^5 - 10^7 M_\odot$ according to Appendix A. The above relationships suggest that the majority of the diffraction events detected by LISA should be induced by small halos, because (i) the lensing probability increases with y^2 and (ii) when y is large only small halos produce strong diffraction effect.

2.2. DM Halos and Subhalos

The lenses of our interest are those DM halos as small as $10^5 - 10^7 M_\odot$. The last section has shown that they induce an observable diffraction effect to the mHz GWs in the LISA band. Two types of DM halos fall in this mass range.

The first type reside in the low-density regions of the universe. They predominate the low-mass end of the mass function of ordinary DM halos (e.g. Wang et al. 2020). To compute the number density of these halos, we adopt the mass function density dn/dM_h derived in Cooray & Sheth (2002), where n denotes the number density of halos in unit of Mpc^{-3} and M_h is the halo mass. Note that by convention dn/dM_h has a unit of $M_\odot^{-1} \text{Mpc}^{-3} h^3$.

The second type of DM halos fall in our interested mass range are the substructures of those massive DM halos. These substructures are often referred to as ‘‘subhalos’’. Numerical simulations show that given the mass M_h of a main halo, the masses of the subhalos follow a power-law distribution with a universal power-law index (e.g. Gao et al. 2004a,b; Diemand et al. 2004; Libeskind et al. 2005; Giocoli et al. 2008)). Following Han et al. (2016), we write the mass function of the subhalos as

$$\frac{dN(< R)}{d \ln m} = A(R) \frac{M(< R)}{m_0} \left[\frac{m}{m_0} \right]^{-\alpha}, \quad (12)$$

where $N(< R)$ is the number of subhalos within a radius of R of the main halo, m is the mass of the subhalo, $A(R)$

is a normalization factor, $M(< R)$ is the total mass enclosed by the radius R , and $m_0 = 10^{10} M_\odot$ and $\alpha = 0.96$ are constants nearly independent of the halo mass or redshift. In the later calculation, we are mainly interested in the number of subhalos within the virial radius R_{vir} of the main halo, regardless of their spatial distribution within the main halo. Therefore, we should replace R with R_{vir} when using Equation (12). By construction, the total mass within the virial radius is $M(< R_{\text{vir}}) = M_h$. This leaves $A(R_{\text{vir}})$ the only quantity that is undetermined. We notice that Figure 15 of Han et al. (2016) gives the value of $A(< R)$ which shows that at $R = R_{\text{vir}}$ the value converges to 0.01 for a wide range of halo mass, from $M_h = 10^{12} h^{-1} M_\odot$ to $10^{15} h^{-1} M_\odot$. For this reason, we adopt $A(< R_{\text{vir}}) = 0.01$ for our later calculations.

Knowing the mass function of subhalos in one main halo, we can calculate the mass function density at a given redshift for all the subhalos of the same mass with

$$\frac{dn_{\text{sub}}}{dm}(m, z_L) = \int dM'_h \frac{dn(M'_h, z_L)}{dM'_h} \frac{dN}{d \ln m} \frac{1}{m}. \quad (13)$$

Such a quantity is useful for our later calculation of the lensing probability. Correspondingly, the total mass function density contributed by the halos and subhalos of a mass of M_h is

$$\xi_{\text{lens}}(M_h, z) = \frac{dn_{\text{sub}}}{dM_h}(M_h, z) + \frac{dn}{dM_h}(M_h, z). \quad (14)$$

Note that to find the lens mass M_L corresponding to a halo mass M_h , the relationship derived in Appendix A is applied.

Figure 3 shows the mass function density predicted by Equation (14). We can see that the mass function density has little evolution from redshift $z = 2$ to 6 (upper panel), and it is more sensitive to the halo mass (lower panel). We note that in general halos are more numerous than subhalos. Nevertheless, we include subhalos in the calculation for completeness.

2.3. Calculation of the Lensing Probability

To calculate the lensing probability, we have to specify (i) the number of lenses of different masses at each redshift and (ii) the solid angle these lenses cover in which we can detect the diffraction of GW.

For (i), we start with the halo mass function density derived in the previous section, $\xi_{\text{lens}}(M_h, z)$. Since the SIS model predicts a unique relationship between the lens mass and halo mass, $M_h(M_L, z_L, z_S)$ (see Appendix A), we can rewrite ξ_{lens} as a function of the lens mass, i.e., $\xi_{\text{lens}}(M_h(M_L, z_L, z_S), z_L)$. Using this

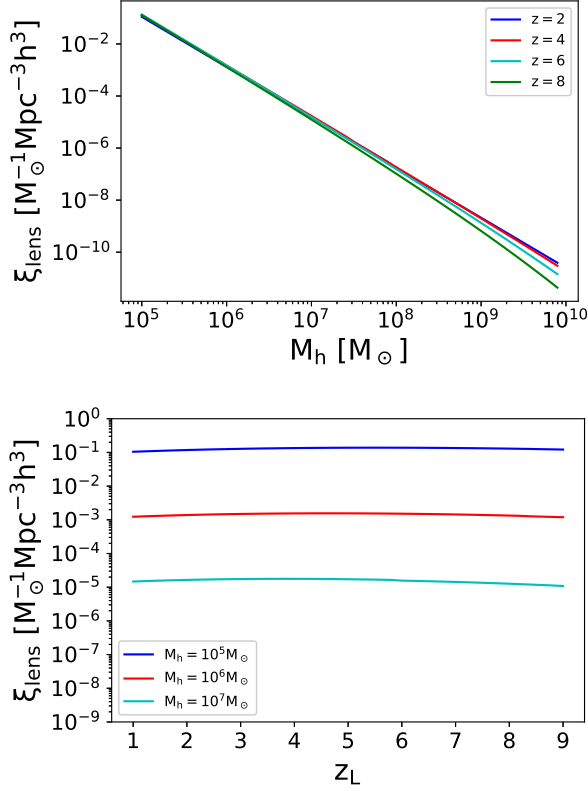


Figure 3. The mass function of the small halos which could produce diffraction effects as a function the halo mass (upper panel) or redshift (lower panel).

new mass function, we can calculate the number of lens in the mass range $(M_L, M_L + dM_L)$ and redshift bin $(z_L, z_L + dz_L)$ per unit solid angle using the equation

$$\frac{d^3 N_{\text{lens}}(M_L, z_L, z_S)}{dM_L dz_L d\Omega} = \xi_{\text{lens}}(M_h(M_L, z_L, z_S), z_L) \times \chi^2(z_L) \frac{d\chi}{dz} \frac{dM_h}{dM_L}, \quad (15)$$

where $\chi(z)$ is the comoving distance for redshift z .

Figure 4 shows the result of Equation (15) integrated over a redshift range of $[0, z_{L\text{max}}]$ and above a certain lens mass. The source is assumed to be at $z_S = 4$. It is clear that the number of lenses in a solid angle increases with redshift, and small lenses (e.g., $M_L \sim 10 M_\odot$) are the most numerous. Therefore, we expect that small halos contribute most of the lensing events. We have considered the lenses as small as $10 M_\odot$ because they correspond to a halo mass of about $10^9 M_\odot$ (see Appendix A).

As for (ii), suppose y_{crit} is the critical impact parameter in the source plane within which the effect due to the diffraction of GW is detectable. In the lens plane, the critical impact parameter corresponds to an angular

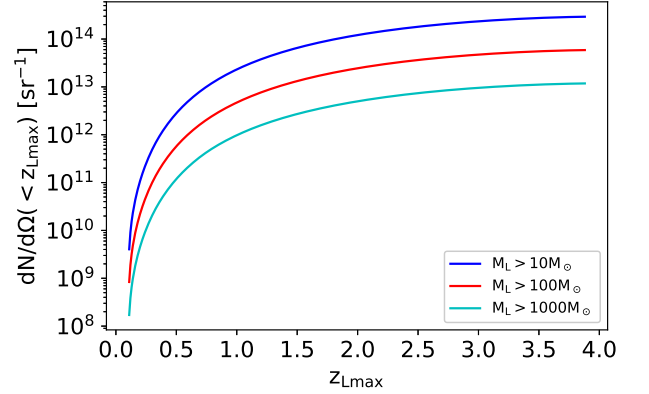


Figure 4. Cumulative distribution of lenses per unit solid angle. The three curves from top to bottom are counting the lenses above three different minimum masses, i.e., $M_{L\text{min}} = (10, 100, 1000) M_\odot$. In this example, the source is at $z_S = 4$.

size of

$$\theta(M_S, M_L, z_L, z_S) = \xi_0 y_{\text{crit}} / D_L. \quad (16)$$

We have written θ as a function of the source mass M_S and redshift z_S to highlight the dependence of y_{crit} on the “loudness” of the source. Therefore, the lensing effect is detectable within a solid angle of

$$\pi\theta^2 = \pi y^2 \times \frac{4GM_L D_{LS}}{c^2 D_L D_S} \quad (17)$$

towards the lens, where we have used the relation

$$\xi_0 = 2\sqrt{GM_L \frac{D_L D_{LS}}{c^2 D_S}} \quad (18)$$

from the SIS model. Summing up all possible lenses between the source and the observer, we derive the lensing probability—the probability of detecting the diffraction effect in a given GW source—as

$$P = \int_0^{z_S} dz_L \int \pi\theta^2 \times \frac{d^3 N_{\text{lens}}(M_L, z_L, z_S)}{dM_L dz_L d\Omega} dM_L. \quad (19)$$

In principle, the integration should be performed over all possible lens masses. In practice, we restrict the integration within a mass range $[M_{L\text{min}}, M_{L\text{max}}]$. The upper and lower limits are functions of lens redshift z_L , which should be determined by evaluating the prominence of the diffraction effect. Only those lenses producing a detectable diffraction effect should be counted. The following subsection explains how we quantify the detectability of the diffraction effect.

2.4. Signal and Matched Filtering

The magnification factor derived in Section 2.1 is a function of GW frequency. To use it, we need to first

derive the unlensed GW signal in the frequency domain. This is done by a Fourier transformation,

$$\tilde{h}(f) = \int e^{2\pi ift} h(t) dt, \quad (20)$$

of the GW strain $h(t)$ in the time domain.

For illustrative purposes, we show in Figure 5 the characteristic strain of three MBH mergers (solid curves). We assume equal-mass mergers for simplicity and the total masses are $M_S = 10^4, 10^5$, and $10^6 M_\odot$ respectively. The source redshift is fixed at $z_S = 4$ in these examples. The waveforms are generated using the “IMRPhenomC” model in the PyCBC package (Santamaría et al. 2010; Nitz et al. 2020), excluding the effect of BH spin. Because we assume circular orbits for the MBH binaries, the merger time is about $1.7 f_{\text{mHz}}^{-8/3} M_4^{-5/3} (1 + z_S)$ years (Peters & Mathews 1963), where f_{mHz} is the GW frequency in unit of mHz and M_4 is the total BH mass in unit of $10^4 M_\odot$. It is shorter than the canonical lifetime of LISA (5 years) except in the case of the smallest BHs.

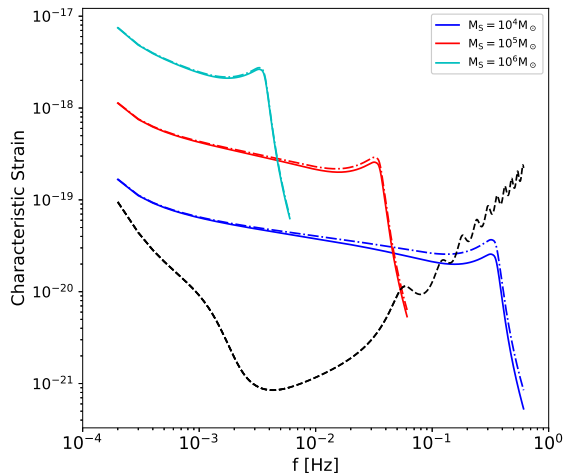


Figure 5. Characteristic strains of unlensed (solid lines) and lensed (dot-dashed lines) MBH binaries. The lines of different colors correspond to different total masses of the binaries. The black dashed line is the square root of the spectral noise density of LISA, i.e., $\sqrt{f S_h(f)}$, adopted from Robson et al. (2019).

We now integrate the characteristic strain in Figure 5 to derive the SNR of each merger. The calculation takes advantage of an inner product (Finn 1992; Cutler & Flanagan 1994) which is defined as

$$\langle h_1 | h_2 \rangle = 2 \int_0^\infty \frac{\tilde{h}_1^*(f) \tilde{h}_2(f) + \tilde{h}_1(f) \tilde{h}_2^*(f)}{S_h(f)} df, \quad (21)$$

where h_1 and h_2 are two waveforms, $S_h(f)$ is the one-sided power spectral density for LISA (from Robson

et al. 2019), and the star symbols denote the complex conjugates. The SNR of a signal h is defined as $\text{SNR} := \sqrt{\langle h | h \rangle}$.

Figure 6 shows the SNR of different MBH mergers at different redshift. We see that when the total mass is higher than about $10^4 M_\odot$ and the source redshift is lower than 10, the source in general has a SNR much higher than 10. These events are detectable by LISA (Amaro-Seoane et al. 2017). In the following we study the lensing signals of these events.

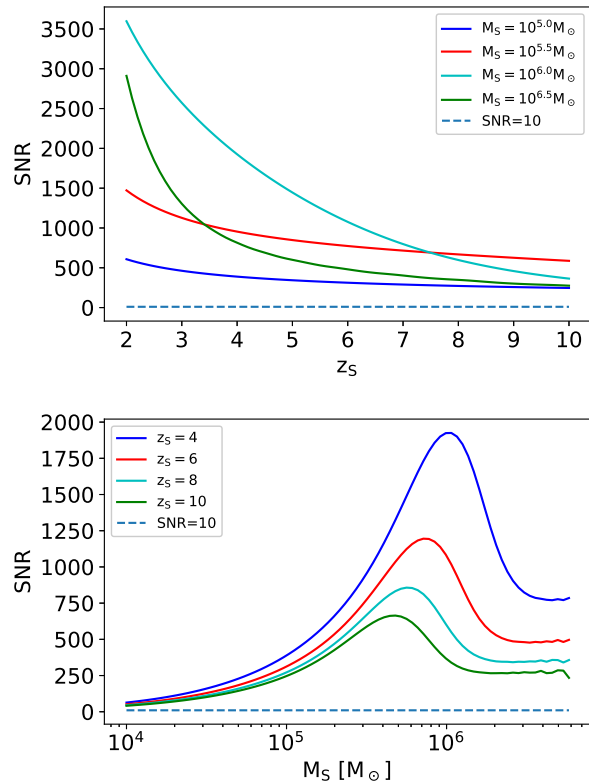


Figure 6. SNR as a function of the redshift (upper panel) or the total mass (lower panel) of the source.

The strain of the lensed signals are shown in Figure 5 as the dot-dashed lines. In the calculation, we assumed that the lens has a mass of $M_L = 10^4 M_\odot$ and is at a redshift of $z_L = 2$. The impact parameter is set to $y = 1$ to maximize the effect in these examples. In this case, we can discern by eye that the lensed signals differ from the unlensed ones.

In more general cases, the impact parameters are much larger than 1 so that the diffraction effects are much more difficult to discern by eye (e.g., see Figure 2). To quantify a small difference between two waveforms, we define $\delta h := h_1 - h_2$. We deem the two waveforms to be discernible when the SNR of the difference

is larger than 1, i.e., $\langle \delta h | \delta h \rangle > 1$ (Lindblom et al. 2008). We are being optimistic in adopting this criterion because we assume that the deviation of the waveform from the theoretical waveform comes completely from the lensing effect. However, when the SNR is high, the criterion can be satisfied due to other factors, such as the presence of other signals, inaccurate waveform template, and the non-Gaussianity/non-stationarity of the noise. (I deleted “the lensing effect from neighbouring (sub)halos” because it is also kind of a lensing signal) Nevertheless, it provides a practical criterion by which we can select from our simulations the lensing events which contain possibly discernible diffraction features.

3. DIFFERENCE BETWEEN LENSED AND UNLENSED SIGNALS

The significance of the diffraction effect on the lensing signal depends on five parameters. Two of them are related to the source, i.e., the total mass of the MBH binary M_S and the source redshift z_S . Two are related to the lens, i.e., the lens mass M_L and redshift z_L . The final one is the impact parameter y . In this section, we investigate the dependence of the inner product $\langle \delta h | \delta h \rangle$ on these parameters.

Figure 7 shows the dependence of $\langle \delta h | \delta h \rangle$ on the source mass M_S . Comparing it with the lower panel of Figure 6, we find that the inner product behaves similarly as the SNR of the unlensed signal. The reason is that higher SNR normally makes it easier to identify the diffraction effect. Moreover, we find that when $M_S \lesssim 10^5 M_\odot$, the inner product becomes smaller than unity. For this reason, we will restrict our later analysis to $M_S \geq 10^5 M_\odot$. Note that we are already considering a relatively conservative example in the sense that the lens mass is small, $M_L = 16 M_\odot$ [so that the term ωM_L in Eq.6 becomes $f(100 M_\odot)$], and the impact parameter is relatively large ($y = 100$). Increasing the lens mass and decreasing the impact parameter could both enhance the inner product to $\langle \delta h | \delta h \rangle > 1$ even when $M_S < 10^5 M_\odot$.

The dependence of $\langle \delta h | \delta h \rangle$ on the lens mass M_L is shown in Figure 8. We see a wave-like behavior of the inner product. It is correlated with the behavior of the amplification factor, as has been shown in Figure 2. As M_L increases to $10^4 M_\odot$, $\langle \delta h | \delta h \rangle$ converges to a constant value which depends on both the source and the lens redshifts. Such a convergence is due to the limit of the geometric optics. For a variety of combinations of z_S and z_L , we find that $\langle \delta h | \delta h \rangle$ becomes smaller than 1 when M_L is smaller than about $10 M_\odot$. This result indicates that such small lenses should not produce a detectable diffraction signature. Therefore, in

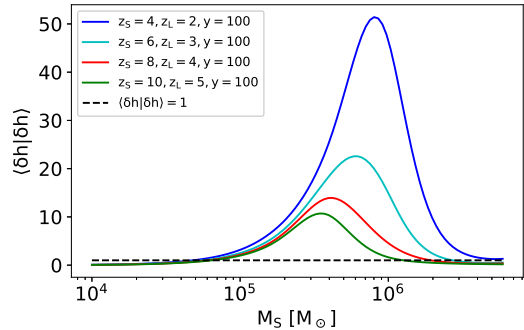


Figure 7. The inner product $\langle \delta h | \delta h \rangle$ as a function of the total mass of the source. The solid lines of different colors correspond to different combinations of source redshift, lens redshift, and impact parameter. The lens mass is fixed to $M_L = 16 M_\odot$ in this example. The black dashed line marks the place where $\langle \delta h | \delta h \rangle = 1$.

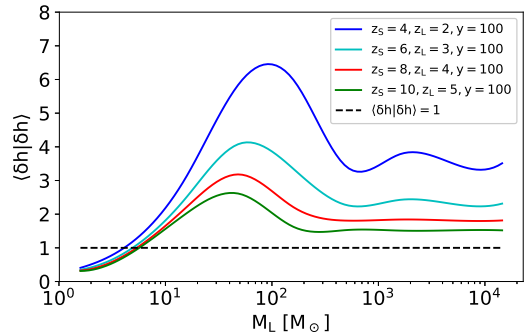


Figure 8. The same as Fig. 7 but varying the lens mass M_L while fixing the source mass at $M_S = 10^5 M_\odot$.

the following we do not consider lens masses significantly smaller than $10 M_\odot$. Moreover, when M_L is significantly greater than $10^5 M_\odot$, the system enters the geometric-optics limit since w starts to exceed $10^{-2}(1+z_L)$ according to Equation (11). In this limit, the amplification factor converges to $\sqrt{1+1/y}$ for all frequencies (Takahashi & Nakamura 2003). As a result, the diffraction effect is suppressed. Therefore, we do not consider the lens masses significantly greater than $10^5 M_\odot$ either.

Figure 9 shows the inner product as a function of the lens redshift. We find that $\langle \delta h | \delta h \rangle$ increases as the lens redshift approaches the source redshift. This behavior is caused by the fact that the lensing effect is in general stronger when the lens and the source are closer. We also find that the sources at higher redshift in general produce a smaller $\langle \delta h | \delta h \rangle$. This result stems from the decrease of the SNR as the source redshift increases.

Finally, we show the dependence of $\langle \delta h | \delta h \rangle$ on the impact parameter y in Figure 10. In general, the inner product decreases with the impact parameter. Interest-

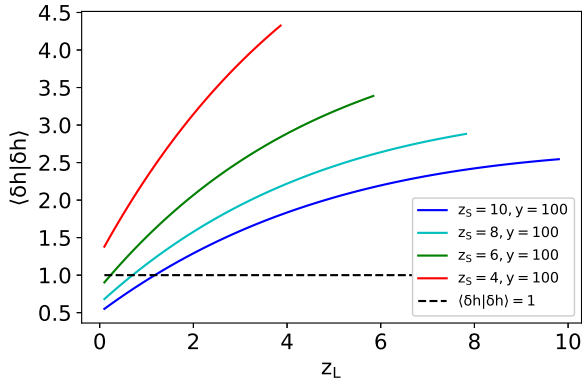


Figure 9. Dependence of the inner product $\langle \delta h | \delta h \rangle$ on the lens redshift z_L . In this example, the source mass is chosen to be $M_S = 10^5 M_\odot$ and the lens mass is $M_L = 16 M_\odot$. The impact parameter is fixed at $y = 100$ for easier comparison.

ingly, for a variety of lensing systems, we find that the inner product remains higher than 1 as long as $y \lesssim 200$. We note that the lensing effect due to such a large impact parameter has not been accounted for previously in the literature.

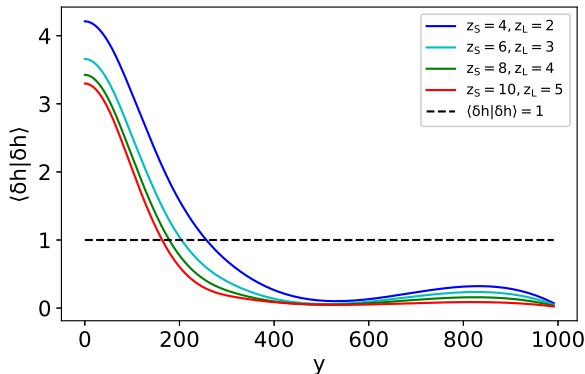


Figure 10. The inner-product $\langle \delta h | \delta h \rangle$ as a function of the dimensionless impact parameter y . In these examples, we have chosen $M_S = 10^5 M_\odot$ and $M_L = 16 M_\odot$.

4. LENSING PROBABILITY

Having understood the dependence of the inner product $\langle \delta h | \delta h \rangle$ on the parameters M_S , z_S , M_L , z_L , and y , we can now include the halo mass function and calculate the probability that a MBH binary in the LISA band has $\langle \delta h | \delta h \rangle > 1$ due to the diffraction effect. We denote this probability as $P(\langle \delta h | \delta h \rangle > 1)$, and the expression can be derived from Equation (19) with a slight modification.

Given (M_S, z_S, M_L, z_L) , we first calculate the critical impact parameter y_{crit} which produces exactly $\langle \delta h | \delta h \rangle = 1$. Figure 11 shows the critical impact parameter as a function of the lens redshift. We can see

that in a large redshift range, y_{crit} is higher than 10^2 . Moreover, sources at lower redshifts have higher y_{crit} , since the SNR is higher.

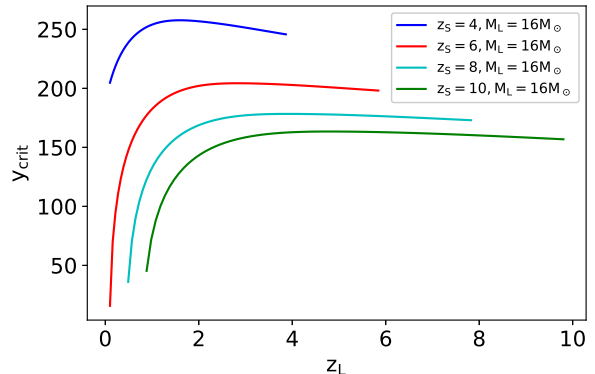


Figure 11. The critical impact parameter which gives $\langle \delta h | \delta h \rangle = 1$ as a function of the lens redshift. Different lines correspond to different source redshift. In the calculation, we fix the lens mass to $16 M_\odot$ and the source mass to $10^5 M_\odot$.

Then we replace θ in the integrand of Equation (19) with $\theta(y_{\text{crit}})$ and integrate to give the probability $P(y < y_{\text{crit}})$. This probability $P(y < y_{\text{crit}})$ is equivalent to $P(\langle \delta h | \delta h \rangle > 1)$. In principle, given the source, i.e., after fixing M_S and z_S , the y_{crit} in the integrand is a function of both z_L and M_L . In practice, we only consider the lenses more massive than $M_L = 16 M_\odot$ because less massive lens in general do not produce a sufficiently large inner product $\langle \delta h | \delta h \rangle$, as Figure 8 has shown. Moreover, to simplify the calculation, we only use the values of y_{crit} computed for a single lens mass $M_L = 16 M_\odot$ (so that $2\pi M_L$ in Eq. 6 becomes $10^2 M_\odot$). The value of $y_{\text{crit}}(M_L = 16 M_\odot)$ can be regarded as the lower limit to y_{crit} , since Figure 8 shows that $M_L > 16 M_\odot$ leads to $\langle \delta h | \delta h \rangle > 1$, which suggests that $y_{\text{crit}}(M_L > 16 M_\odot)$ is greater than $y_{\text{crit}}(M_L = 16 M_\odot)$. Correspondingly, the lensing probability derived with $y_{\text{crit}}(M_L = 16 M_\odot)$ is a lower limit as well. Note that although we fix M_L when calculating $y_{\text{crit}}(M_L)$, we do not fix the value of M_L in the halo mass function of Equation (19).

These lower limits of the lensing probability are given in Table 1. We restrict M_L to the mass range $[16, 1.6 \times 10^4] M_\odot$ because, as has been mentioned above, neither the smaller lenses nor the larger ones produce significant diffraction effect. The corresponding halo mass is between 10^5 and $10^7 M_\odot$. In the calculation, we assume that the total source mass is $M_S = 10^5 M_\odot$ and we find that the total probability is 0.28, 0.34, 0.37, and 0.40 for a source at $z_S = 4, 6, 8, 10$. The lensing probability would be even higher if we adopt a source mass of

Table 1. Lensing Probability Contributed by Different Lenses

z_S	4	6	8	10
$P(M_L = 1.6 \times 10^1 \sim 1.6 \times 10^2 M_\odot)$	0.04	0.05	0.05	0.06
$P(M_L = 1.6 \times 10^2 \sim 1.6 \times 10^3 M_\odot)$	0.08	0.10	0.11	0.11
$P(M_L = 1.6 \times 10^3 \sim 1.6 \times 10^4 M_\odot)$	0.16	0.19	0.21	0.23
$P(M_L = 1.6 \times 10^1 \sim 1.6 \times 10^4 M_\odot)$	0.28	0.34	0.37	0.40

$M_S = 10^6 M_\odot$ because the inner product $\langle \delta h | \delta h \rangle$ would be greater, as is shown in Figure 7. However, for a source mass of $10^7 M_\odot$ or higher, the lensing probability would be lower than those given in Table 1, because Figure 7 shows that the corresponding inner product is smaller than 1. The above results indicate that for those MBHs in the mass range between $10^5 M_\odot$ and $10^6 M_\odot$, it is probable that LISA could detect the diffraction effect.

Table 1 also shows that the biggest contribution to the lensing probability comes from the lenses within the highest mass range, between 1.6×10^3 and 1.6×10^4 . These lenses are the least abundant according to Figure 3. Nevertheless, their contribution is the largest because their strong gravity leads to a large lensing cross section.

5. IMPACT OF DM MODELS

We notice that Takahashi & Nakamura (2003) derived a lensing probability of $10^{-4} \sim 10^{-3}$ for the MBH binaries in the LISA band. It is two to three orders of magnitude smaller than our estimation. The discrepancy stems from the different mass range of the lenses that are considered in the two works.

Takahashi & Nakamura (2003) considered the lenses in the mass range of $M_L = 10^6 \sim 10^9 M_\odot$, which corresponds to a halo mass of $10^9 \sim 10^{12} M_\odot$. Note that such lenses are already in the geometric-optics limit. Moreover, they assumed a critical impact parameter of $y_{\text{crit}} = 3$. In our model, we considered the lenses in the mass range of $16 \sim 1.6 \times 10^4 M_\odot$. The corresponding halo mass is $10^5 \sim 10^8 M_\odot$. These lenses produce wave-optics effect in the lensing signal, and we have shown that the effect is detectable even for a large impact parameter of $y \sim 200$ (Figure 11).

The difference of the lens masses produces two consequences in the estimation of the lensing probability. (i) In our model, the solid angle within in which the lensing signal is detectable is about 20 times smaller than the choice of Takahashi & Nakamura (2003), since it is proportional to $y_{\text{crit}}^2 M_L$ according to Equation (17). (ii) Our lenses are 2000 \sim 2500 times more numerous than those considered in Takahashi & Nakamura (2003) according to Figure 3. The difference can be more clearly

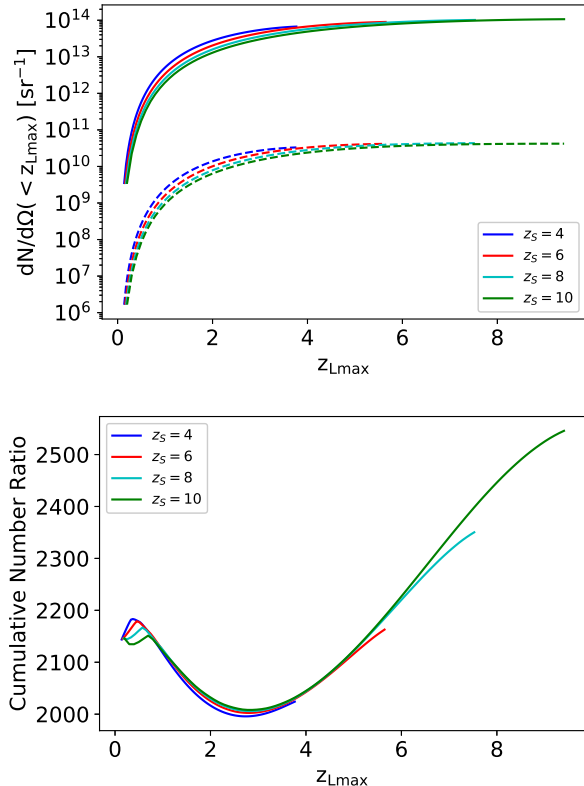


Figure 12. Upper panel: Cumulative distribution of the number of lenses as a function of the upper limit of lens redshift z_{Lmax} . The solid lines represent the lenses in the mass range of $M_L = 16 \sim 1.6 \times 10^4 M_\odot$, while the dashed one represent the lenses of $10^6 \sim 10^9 M_\odot$. The four colors refer to four different source redshifts. Lower panel: The ratio between the two kinds of cumulative lens numbers.

seen in Figure 12. Given these two consequences, we can understand the result that our lensing probability is about 100 times higher than that derived in Takahashi & Nakamura (2003).

The above comparison suggests that the lensing probability is sensitive to the abundance of small halos. Since different DM models predict very different number density for small halos, we now investigate the dependence of the lensing probability on the lower boundary of the halo mass function. To simulate the effect of different DM models, we cut off the integration of Equation (19) at different lower boundaries M_{hmin} and count only those halo with $M_h > M_{hmin}$. The result is shown in Figure 13. We see a sharp cut off around $M_{hmin} = 10^8 M_\odot$. This result indicates that LISA is unlikely to detect the diffraction effect of a MBH binary if the smallest halos are all above $10^8 M_\odot$, as the warm-DM models would predict (e.g. Lovell et al. 2014).

6. SUMMARY CONCLUSION

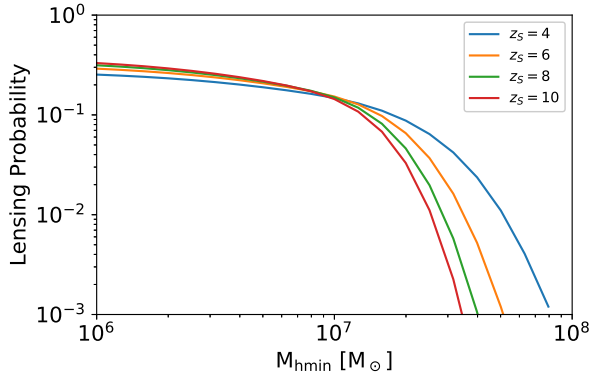


Figure 13. The total lensing probability as a function of the minimum halo mass. Different colors refer to difference source redshift.

In this work, we studied the lensing signals of the MBH binaries in the LISA band. We focus on the wave-optics effect and found that it is produced mainly by the DM halos and subhalos in the mass range of $10^5 \sim 10^8 M_\odot$. Using the matched-filtering technique, we showed that the effect could be discernible by LISA even when the source has an impact parameter as large as $y = 200$. Such a large impact parameter substantially enhances the probability of detecting the diffraction signatures. According to our preliminary estimation, if CDM predominates the matter content of the universe, we could already detect the diffraction effect after 3 – 4 MBH binaries in the mass range of $10^5 \sim 10^6 M_\odot$ are discovered by LISA. If, on the other hand, warm DM predominates, the chance of detecting the diffraction effect would be diminished by at least one order of magnitude. Therefore, looking for the wave-optics effects in LISA events could help us constrain the DM models.

APPENDIX

A. RELATION BETWEEN HALO MASS AND LENS MASS IN THE SIS MODEL

We assume that DM halo follows an SIS density profile,

$$\rho(r) = \frac{\sigma_v^2}{2\pi G r^2}, \quad (\text{A1})$$

where σ_v is the velocity dispersion. According to this profile, the total mass of the halo, M_h , is related to the virial radius $r_{\text{vir}}(M_h, z_h)$, which is a function of the mass M_h and redshift z_h , as

$$M_h = \frac{2\sigma_v^2}{G} r_{\text{vir}}(M_h, z_h). \quad (\text{A2})$$

The lens mass is defined as the mass enclosed by a circle on the lensing plane with a radius of $\xi_0 = 4\pi\sigma_v^2 D_L D_{LS}/c^2 D_S$, which is known as the Einstein radius. To calculate the lens mass M_L , we use the the surface density of an SIS projected on the lensing plane, $\Sigma(\xi) = \sigma_v^2/(2G\xi)$ (Takahashi & Nakamura 2003), and derive

$$M_L = \frac{4\pi^2\sigma_v^4 D_L D_{LS} D_L}{G D_S c^2}. \quad (\text{A3})$$

As a final remark, we note that our model of the lensing signal and the criterion of discerning the diffraction effect are based on ideal assumptions. For example, we do not consider multiple lenses along the line of sight even though we have found a relatively high lensing probability. Moreover, we have assumed that the deviation of the detected signal from the model template is solely due to gravitational lensing, while for real LISA observation, other factors, such as confusion between multiple events or inaccuracy of the waveform template, could also contribute to the deviation. We will address these caveats in a future work.

ACKNOWLEDGMENTS

This work is supported by the National Science Foundation of China grants No 11873022, 11991053, and 11805286. X.C. is partly supported by the Strategic Priority Research Program of the Chinese Academy of Sciences, Grant No. XDB23040100 and No. XDB23010200. Y.H. is partly supported by the National Key Research and Development Program of China (No. 2020YFC2201400), and Guangdong Major Project of Basic and Applied Basic Research (Grant No. 2019B030302001). We especially thank Liang Dai at University of California, Berkeley for many insightful discussions on the theory of wave-optical lensing model and precious comments on an early version of this manuscript. We also extremely thank Xiao Guo at National Astronomical Observatories of China (NAOC) for providing us with valuable suggestions on various problems encountered in this work.

To relate the halo mass to the lens mass, we use Equations (A2) and (A3) to eliminate σ_v and we find that

$$M_h = r_{\text{vir}}(M_h, z_h) \sqrt{\frac{M_L D_S c^2}{\pi^2 G D_{LS} D_L}}. \quad (\text{A4})$$

Figure 14 shows the relationship between these two masses and the dependence on the redshift of the halo.

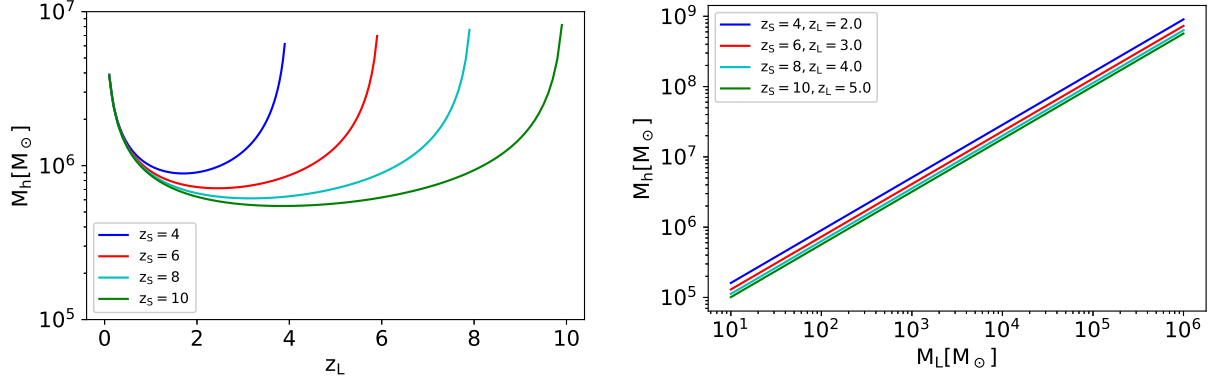


Figure 14. The left panel shows the halo mass as a function of the redshift when the lens mass is fixed to $100 M_\odot$. Different lines correspond to different redshift of the source. The right panel shows the halo mass as a function of lens mass M_L . Different lines correspond to different combinations of the source and lens redshifts.

REFERENCES

- Abbott, B. P., Abbott, R., Abbott, T. D., et al. 2016, *Phys. Rev. Lett.*, 116, 131103, doi: [10.1103/PhysRevLett.116.131103](https://doi.org/10.1103/PhysRevLett.116.131103)
- . 2019, *Phys. Rev. X*, 9, 031040, doi: [10.1103/PhysRevX.9.031040](https://doi.org/10.1103/PhysRevX.9.031040)
- Abbott, R., Abbott, T. D., Abraham, S., et al. 2020, arXiv e-prints, arXiv:2010.14527. <https://arxiv.org/abs/2010.14527>
- Amaro-Seoane, P., Audley, H., Babak, S., et al. 2017, arXiv e-prints, arXiv:1702.00786. <https://arxiv.org/abs/1702.00786>
- Bontz, R. J., & Haugan, M. P. 1981, *Ap&SS*, 78, 199, doi: [10.1007/BF00654034](https://doi.org/10.1007/BF00654034)
- Cao, Z., Li, L.-F., & Wang, Y. 2014, *PhRvD*, 90, 062003, doi: [10.1103/PhysRevD.90.062003](https://doi.org/10.1103/PhysRevD.90.062003)
- Christian, P., Vitale, S., & Loeb, A. 2018, *PhRvD*, 98, 103022, doi: [10.1103/PhysRevD.98.103022](https://doi.org/10.1103/PhysRevD.98.103022)
- Cooray, A., & Sheth, R. 2002, *Physics Reports*, 372, 1–129, doi: [10.1016/s0370-1573\(02\)00276-4](https://doi.org/10.1016/s0370-1573(02)00276-4)
- Cusin, G., & Lagos, M. 2020, *PhRvD*, 101, 044041, doi: [10.1103/PhysRevD.101.044041](https://doi.org/10.1103/PhysRevD.101.044041)
- Cutler, C., & Flanagan, E. E. 1994, *Phys. Rev. D*, 49, 2658
- Cyranowski, J. F. 1974, PhD thesis, Wisconsin Univ., Milwaukee
- Dai, L., Li, S.-S., Zackay, B., Mao, S., & Lu, Y. 2018, *PhRvD*, 98, 104029, doi: [10.1103/PhysRevD.98.104029](https://doi.org/10.1103/PhysRevD.98.104029)
- Diego, J. M., Hannuksela, O. A., Kelly, P. L., et al. 2019, *A&A*, 627, A130, doi: [10.1051/0004-6361/201935490](https://doi.org/10.1051/0004-6361/201935490)
- Diemand, J., Moore, B., & Stadel, J. 2004, *Monthly Notices of the Royal Astronomical Society*, 352, 535–546, doi: [10.1111/j.1365-2966.2004.07940.x](https://doi.org/10.1111/j.1365-2966.2004.07940.x)
- Finn, L. S. 1992, *PhRvD*, 46, 5236, doi: [10.1103/PhysRevD.46.5236](https://doi.org/10.1103/PhysRevD.46.5236)
- Gao, L., De Lucia, G., White, S. D. M., & Jenkins, A. 2004a, *Monthly Notices of the Royal Astronomical Society*, 352, L1–L5, doi: [10.1111/j.1365-2966.2004.08098.x](https://doi.org/10.1111/j.1365-2966.2004.08098.x)
- Gao, L., White, S. D. M., Jenkins, A., Stoehr, F., & Springel, V. 2004b, *Monthly Notices of the Royal Astronomical Society*, 355, 819–834, doi: [10.1111/j.1365-2966.2004.08360.x](https://doi.org/10.1111/j.1365-2966.2004.08360.x)
- Giocoli, C., Tormen, G., & van den Bosch, F. C. 2008, *Monthly Notices of the Royal Astronomical Society*, 386, 2135–2144, doi: [10.1111/j.1365-2966.2008.13182.x](https://doi.org/10.1111/j.1365-2966.2008.13182.x)
- Han, J., Cole, S., Frenk, C. S., & Jing, Y. 2016, *Monthly Notices of the Royal Astronomical Society*, 457, 1208–1223, doi: [10.1093/mnras/stv2900](https://doi.org/10.1093/mnras/stv2900)
- Hannuksela, O. A., Haris, K., Ng, K. K. Y., et al. 2019, *The Astrophysical Journal*, 874, L2, doi: [10.3847/2041-8213/ab0c0f](https://doi.org/10.3847/2041-8213/ab0c0f)
- Hou, S., Li, P., Yu, H., et al. 2020, arXiv e-prints, arXiv:2009.08116. <https://arxiv.org/abs/2009.08116>
- Jung, S., & Shin, C. S. 2019, *PhRvL*, 122, 041103, doi: [10.1103/PhysRevLett.122.041103](https://doi.org/10.1103/PhysRevLett.122.041103)
- Lawrence, J. K. 1971, *Nuovo Cimento B Serie*, 6B, 225, doi: [10.1007/BF02735388](https://doi.org/10.1007/BF02735388)
- Liao, K., Biesiada, M., & Fan, X.-L. 2019, *ApJ*, 875, 139, doi: [10.3847/1538-4357/ab1087](https://doi.org/10.3847/1538-4357/ab1087)
- Libeskind, N. I., Frenk, C. S., Cole, S., et al. 2005, *Monthly Notices of the Royal Astronomical Society*, 363, 146–152, doi: [10.1111/j.1365-2966.2005.09425.x](https://doi.org/10.1111/j.1365-2966.2005.09425.x)
- Lindblom, L., Owen, B. J., & Brown, D. A. 2008, *PhRvD*, 78, 124020, doi: [10.1103/PhysRevD.78.124020](https://doi.org/10.1103/PhysRevD.78.124020)
- Lovell, M. R., Frenk, C. S., Eke, V. R., et al. 2014, *Monthly Notices of the Royal Astronomical Society*, 439, 300–317, doi: [10.1093/mnras/stt2431](https://doi.org/10.1093/mnras/stt2431)
- Marković, D. 1993, *PhRvD*, 48, 4738, doi: [10.1103/PhysRevD.48.4738](https://doi.org/10.1103/PhysRevD.48.4738)
- Meena, A. K., & Bagla, J. S. 2020, *MNRAS*, 492, 1127, doi: [10.1093/mnras/stz3509](https://doi.org/10.1093/mnras/stz3509)
- Mei, J., et al. 2020, doi: [10.1093/ptep/ptaa114](https://doi.org/10.1093/ptep/ptaa114)
- Moylan, A. J., McClelland, D. E., Scott, S. M., Searle, A. C., & Bicknell, G. V. 2008, in *The Eleventh Marcel Grossmann Meeting On Recent Developments in Theoretical and Experimental General Relativity, Gravitation and Relativistic Field Theories*, 807–823, doi: [10.1142/9789812834300_0038](https://doi.org/10.1142/9789812834300_0038)
- Nakamura, T. T. 1998, *PhRvL*, 80, 1138, doi: [10.1103/PhysRevLett.80.1138](https://doi.org/10.1103/PhysRevLett.80.1138)
- Nakamura, T. T., & Deguchi, S. 1999, *Progress of Theoretical Physics Supplement*, 133, 137, doi: [10.1143/PTPS.133.137](https://doi.org/10.1143/PTPS.133.137)
- Nitz, A., Harry, I., Brown, D., et al. 2020, *gwastro/pycbc: PyCBC release v1.16.11*, v1.16.11, Zenodo, doi: [10.5281/zenodo.4075326](https://doi.org/10.5281/zenodo.4075326)
- Oguri, M., & Takahashi, R. 2020, *ApJ*, 901, 58, doi: [10.3847/1538-4357/abafab](https://doi.org/10.3847/1538-4357/abafab)
- Ohanian, H. C. 1974, *International Journal of Theoretical Physics*, 9, 425, doi: [10.1007/BF01810927](https://doi.org/10.1007/BF01810927)
- Peters, P. C., & Mathews, J. 1963, *Physical Review*, 131, 435, doi: [10.1103/PhysRev.131.435](https://doi.org/10.1103/PhysRev.131.435)
- Robson, T., Cornish, N. J., & Liu, C. 2019, *Classical and Quantum Gravity*, 36, 105011, doi: [10.1088/1361-6382/ab1101](https://doi.org/10.1088/1361-6382/ab1101)
- Santamaría, L., Ohme, F., Ajith, P., et al. 2010, *PhRvD*, 82, 064016, doi: [10.1103/PhysRevD.82.064016](https://doi.org/10.1103/PhysRevD.82.064016)

- Schneider, P., Ehlers, J., & Falco, E. E. 1992, *Gravitational Lenses* (New York: Springer),
doi: [10.1007/978-3-662-03758-4](https://doi.org/10.1007/978-3-662-03758-4)
- Sonnabend, D. 1979, PhD thesis, Stanford Univ., CA.
- Takahashi, R. 2004, *A&A*, 423, 787,
doi: [10.1051/0004-6361:20040212](https://doi.org/10.1051/0004-6361:20040212)
- . 2006, *ApJ*, 644, 80, doi: [10.1086/503323](https://doi.org/10.1086/503323)
- . 2017, *ApJ*, 835, 103, doi: [10.3847/1538-4357/835/1/103](https://doi.org/10.3847/1538-4357/835/1/103)
- Takahashi, R., & Nakamura, T. 2003, *The Astrophysical Journal*, 595, 1039–1051, doi: [10.1086/377430](https://doi.org/10.1086/377430)
- Wang, J., Bose, S., Frenk, C. S., et al. 2020, *Nature*, 585, 39–42, doi: [10.1038/s41586-020-2642-9](https://doi.org/10.1038/s41586-020-2642-9)
- Yamamoto, K. 2005, *PhRvD*, 71, 101301,
doi: [10.1103/PhysRevD.71.101301](https://doi.org/10.1103/PhysRevD.71.101301)
- Yoo, C.-M., Nakao, K.-i., Kozaki, H., & Takahashi, R. 2007, *ApJ*, 655, 691, doi: [10.1086/510011](https://doi.org/10.1086/510011)